Fatigue life prediction of welded joints at sub-zero temperatures using modified Paris–Erdogan parameters

Nils-Erik Sanhen [a,b,*], Moritz Braun [b]

[a] *Hamburg University of Technology, Am Schwarzenberg-Campus 4, Hamburg, Germany*
[b] *German Aerospace Center (DLR), Institute of Maritime Energy Systems, Max–Planck-Str. 2, Geesthacht, Germany*

ARTICLE INFO

ABSTRACT

The fatigue life of welded steel components is usually determined by the weldment; in these cases, fracture mechanical approaches are widely used for their prediction. Ferritic steels are known to have a fatigue strength that is dependent on temperature. Therefore, this study evaluates fatigue tests of cruciform joints and transverse stiffeners at different sub-zero temperature levels regarding fatigue life. Simultaneously, the stress intensity factors over the crack length are calculated for the individual experiments using analytical solutions. Then, using the Paris–Erdogan relation with temperature- and material-specific C and m parameters as well as tabular values, the fatigue lives are calculated with analytical solutions and compared with the experimental results. It is shown that the prediction accuracy is significantly increased for the sub-zero temperature range by using temperature-adjusted Paris–Erdogan parameters, as long as the temperature is above the fatigue transition temperature.

1. Introduction

The transition of energy supply systems to renewable energies is closely interwoven with the need for the widest possible geospatial distribution of generation capacities to be able to compensate for local fluctuations. One example of this is the installation of offshore wind turbines off the coasts of the Nordic countries; the harsh climatic conditions must be taken into account in the design and dimensioning of the structures. It is known that the material properties, including fatigue behaviour, of ferritic steels and their weldments at sub-zero temperatures, differ from those at room temperature (RT) [1]. A well-designed structure is one that endures the loads that occur over its intended lifespan with minimal over-dimensioning. For this purpose, it is necessary to consider the changed material behaviour at sub-zero temperatures.

Until the 2010s, the safety of ferritic steels against brittle fracture was the primary concern for low temperature applications. Because if the temperature falls below a certain threshold the fracture mode of ferritic steels changes from ductile shear-dominated to brittle cleavage-dominated. The temperature level defining this threshold is the ductile-to-brittle transition temperature (DBTT) [1]. To ensure that the Ductile to Brittle Transition (DBT) does not occur, fracture toughness criterions are considered, but the changes in fatigue behaviour at sub-zero temperatures are not considered further. The Lloyd's Register FDA ICE Fatigue Induced by Ice Loading procedure, for example, states that the fatigue strength of welded joints is not lower than at RT and the same design curves can be used [2]. This is because in the underlying study no significant difference in fatigue strength could be found between the temperature levels, whereby the number of experiments conducted in the study was small [3]. In recent years, however, there have been an increasing number of publications with more extensive data sets that have dealt with the changing fatigue properties of ferritic steels at sub-zero temperatures, to mention here Alvaro et al. [1] and Braun [4].

One finding of this research is that a significant decrease of the fatigue crack growth (FCG) in ferritic steels with the temperature occurs, until a so-called fatigue transition temperature (FTT) is undershot [5]. Whereby the FTT is at a lower temperature level than the DBTT. Therefore, the transition from a ductile-to-brittle transition differs between static and dynamic failure modes and the positive effects of the lower FTT are neglected.

The fatigue life of structures can be determined by fracture mechanical methods, conventionally a linear relationship is assumed between crack growth per load cycle and the stress intensity at the fracture front. This relationship can be described by formulas according to Paris–Erdogan, these formulas and associated constants describing the material behaviour are part of international codes, such as IIW or BS7910. However, the Paris–Erdogan constants of the codes do not take into account the changing effect of sub-zero temperatures of ferritic steels [6,7].

---

* Corresponding author at: Hamburg University of Technology, Am Schwarzenberg-Campus 4, Hamburg, Germany.
  E-mail addresses: nils-erik.sanhen@tuhh.de (N.-E. Sanhen), moritz.braun@dlr.de (M. Braun).
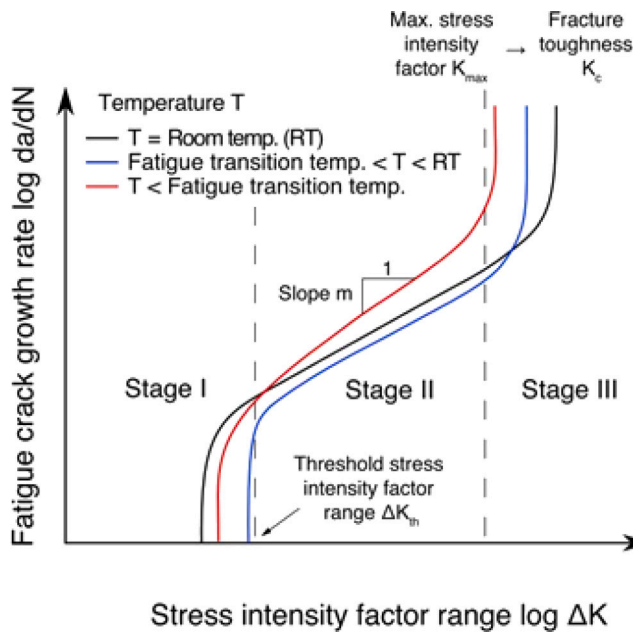
Fig. 1. Schematic representation of fatigue crack growth behaviour below and above the FTT temperature when compared to RT [4].

This work aims to check whether the prediction accuracy of the fatigue life decreases at different sub-zero temperature levels when Paris–Erdogan parameters for RT are used. In addition, it will be examined whether the prediction accuracy can be improved in the sub-zero temperature range by using the material- and temperature-specific Paris–Erdogan parameters. To verify the assumptions, fatigue experiments are carried out with C-joints and transverse stiffeners, the experimentally determined fatigue lives are then compared with predicted fatigue lives.

2. State of the art

2.1. Temperature dependent crack growth behaviour

If the temperature of ferritic steels falls below a threshold the static fracture mode changes from ductile shear-dominated to brittle cleavage-dominated [1]. This ductile-to-brittle transition temperature (DBTT) is defined by a fracture toughness criterion based on a Charpy impact test. Specifically, this is the temperature at which a standardised specimen of the material breaks under an energy of 27J, denoted as the T_{27J} criterion [8]. With regard to fatigue fracture behaviour, there are also effects related to sub-zero temperatures. The decreasing temperature is accompanied by a decrease in the fatigue crack growth (FCG) rate, which increases the number of cycles a structure can endure until the final failure occurs [3]. Similar to the DBTT for the static fracture mode, there is a transition from ductile to brittle dominated effects for fatigue fracture, the fatigue ductile–brittle transition (FDBT). Whereas the FCG rate above the fatigue transition temperature (FTT) decreases, the FCG rate below the FTT accelerates, see Fig. 1 [9].

There is a relationship between the FTT and the DBTT, at the present, this is only described empirically, Alvaro et al. stipulate [10]:

$$FTT = T_{27J} - 15\ °C \tag{1}$$

2.2. Different microstructures in weldments

The welding procedure causes changes in the microstructure of the steel through heat input, the melting and solidification processes. It is possible to distinguish three superordinate types of microstructures,

base material (BM), weld material (WM) and the heat affected zone (HAZ), see Fig. 2[11].

According to Zerbst et al. the HAZ can be further separated into several subzones with different microstructures [11]. The microstructures show different material properties, e.g., values for the T_{27J} criterion and FCG rates. While for cracks originating from the weld root the entire crack grows until the final failure is taking place in WM, cracks originating from the weld toe grow through different zones. Crack initiation is typically assumed to initiate at the fusion line between WM and HAZ, and is extending from the HAZ in the BM [12] In contrast to the homogeneous microstructures of the BM and WM, material properties for the HAZ are scarce and it is difficult to consider their inhomogeneities in fracture mechanical investigations. For a similar study, Song et al. have made the simplifying assumption that crack propagation is completely carried out through BM and the HAZ is not further considered [12].

2.3. Analytical crack growth model

For most types of weldments, the crack initiation period is negligible due to crack like imperfections and sharp notches at weld transitions, the majority of fatigue life takes place in the crack growth period [13,14]. To determine the number of cycles to final failure N_f the crack growth rate da/dN is used. A simple and commonly used form to calculate da/dN is the Paris–Erdogan equation [15]:

$$\frac{da}{dN} = C * (\Delta K)^m \tag{2}$$

The material properties in the Paris–Erdogan equation are described by the parameters C and m, e.g., resulting from changed material properties due to sub-zero temperatures. Paris–Erdogan parameters are defined in international codes, such as IIW or BS7910 [6,7]. To determine the fatigue life of a specimen, the crack propagation rates da/dN is calculated stepwise from the initial crack depth a_i to the final crack depth a_f using the Paris–Erdogan equation:

$$N_f = \int_{a_i}^{a_f} \frac{da}{C * (\Delta K)^m} \tag{3}$$

To solve the equation, the range of the stress intensity factor (SIF) ΔK is required. A formula for the SIF range is:

$$\Delta K_I = \Delta\sigma * \sqrt{\pi * a} * M_k * M \tag{4}$$

The index number I denotes the SIF range as resulting from the opening mode I. The crack growth can be separated into three opening modes, whereby the cracking process is generally in mode I if the loading direction is not changing [16]. The parameters M and M_k are magnification factors, they represent the influences of the weld geometry on the SIFs and are the results of analytical standard solutions. The parameter M describes the factor for a crack in a plain plate and M_k the specific case [17]. The parametric standard solutions, their validity range and the boundary conditions are depicted in standards and recommendations like BS7910 or IIW [6,7]. To determine the magnification factors for a specific case the geometric parameters defining the weldments and a stress range $\Delta\sigma$ are needed. The geometric parameters for the analytical solutions are shown in Fig. 3 for the two in this study investigated weldment types (a) transversal stiffener and (b) a cruciform joint (C-joint).

2.4. Analytical solutions for cruciform joints

In this study, C-joints with the failure location at the weld root should be investigated. For this failure, the crack is initiated due to the non-welded gap between the plates and propagates through the weldment until the final failure occurs. The non-welded gap affects the fatigue behaviour like an initial crack and can be regarded as such. Therefore, at the start of macro crack growth, a continuous crack front is present and the analytical solutions describe a 2D case. The
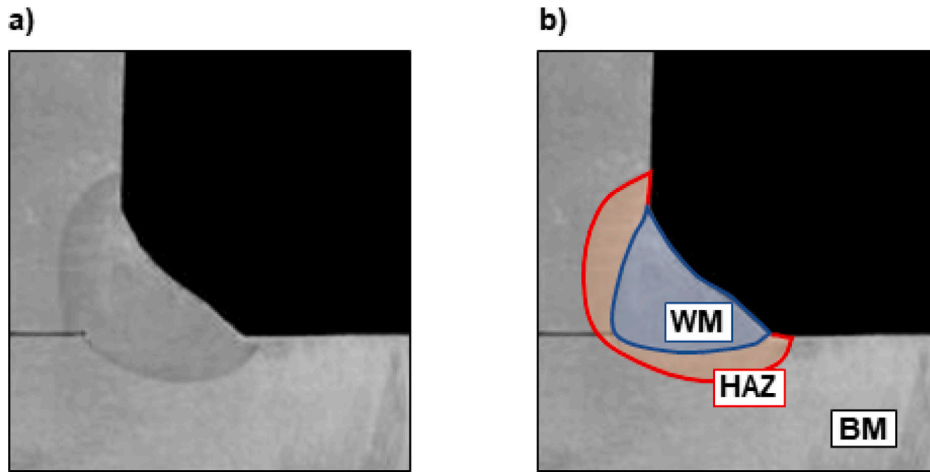
Fig. 2. Superordinate microstructures zones in a weldment.
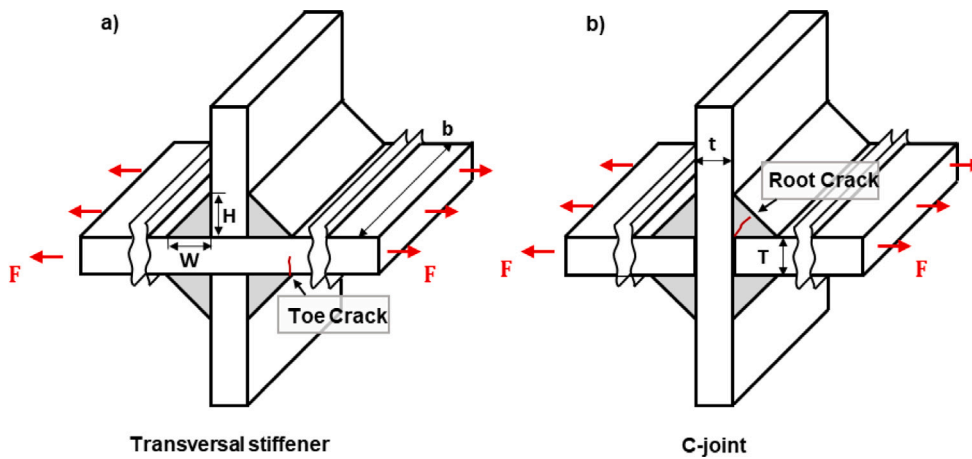

Fig. 3. Sketch with geometric parameters (a) transversal stiffener with toe failure (b) C-joint with root failure.

initial crack depth is half the thickness of the loaded plate $a_i = T/2$. The final depth occurs when the stress intensity factor K_I reaches the fracture toughness K_{Ic}. The fracture toughness is a material property and is dependent on the ambient temperature. Since the majority of the fatigue life takes place during the initial crack growth steps, the final crack depth is less significant. To reduce the calculation effort an alternative stop criterion, described in the IIW Recommendations, can be used. It stipulates that the final failure occurs after the crack has grown through half the plate thickness [6]. For the weldments failing at the root, this criterion is not possible, because the crack is not propagating perpendicular to the surface of the weldment. But following the crack patterns in Braun et al. the crack direction deviates approximately 10° to 15° from the non-welded gap [18]. Based on the final failure criterion from the IIW recommendations $a_f = T/2$, the final crack depth is defined as half the height of a weldment $a_f = a_i + H/2$. For the described case BS7910 defines the plain plate magnification factor as $M = 1$ and the definition for the specific magnification factor M_k can be seen in the following, the formulas for the coefficients λ_0, λ_1 and λ_2 are in Appendix B [7]:

$$M_k = \lambda_0 + \lambda_1 * \left(\frac{2a}{T + 2H} \right) + \lambda_2 * \left(\frac{2a}{T + 2H} \right)^2 \tag{5}$$

2.5. Analytical solutions for transverse stiffener

The second weldment type to be investigated in this study is a transverse stiffener. Macro crack growth starts from one or multiple initial defects or sharp notch tips at the weld toe and grows through

the plate until the final failure occurs at around half the plate thickness $a_f = T/2$. For the initial crack depth $a_i = 0.1$ mm is recommended [6]. Initial defects are typically growing in a semi-elliptical shape first and after a specific crack depth they coalesce to an approximately straight crack front. Therefore, the analytical solutions for semi-elliptical crack growth have to describe the 3D space and not the 2D space. In the 3D calculations alongside with the crack depth a, the crack width c has to be considered, see Fig. 4. The fundamental formula for the 2D and 3D cases remains the same, see Formula (4). The definition of the 3D standard solutions for M and M_k are in Appendices C–E. With the magnification factors SIFs for different angles in the semi-elliptical crack front can be calculated, in the following, only the SIFs at the deepest point are considered.

For the calculation of the magnification factors, a relation between crack depth a and crack width c is needed, the aspect ratio a/c. The aspect ratio can be calculated by determining the growth of the crack in depth and width after a predefined cycle increment ΔN, see [17]. Whereby this procedure requires the calculation of the Paris–Erdogan formula for every increment, which is difficult to combine with the scope of this study to assess the suitability of the Paris–Erdogan parameters. An alternative approach is to use formulas from literature which describe the aspect ratio relation. With these formulas, the magnification factors of a geometry over the entire crack depth a for a constant step width da can be calculated; the Paris–Erdogan formula is not needed. One formula listed in the IIW recommendations based on a linear relation proposed by Engesvik and Moan is [6,19]:
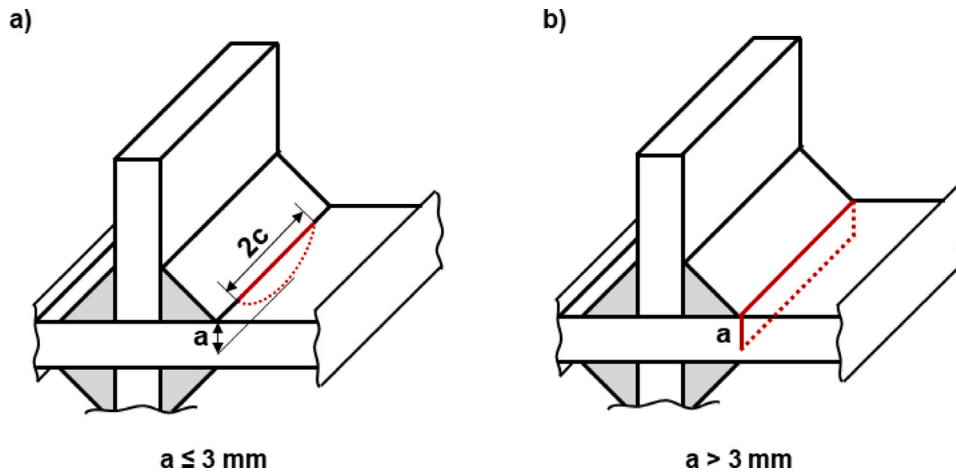
$$2 * c = 6.34 * a - 0.27 \tag{6}$$

Fig. 4. Sketch of a transverse stiffener (a) with a quarter elliptical crack at the weld toe (b) with a continuous crack front at the weld toe.

$$\frac{a}{2} * c = 0; if \ a > 3 \ mm \tag{7}$$

Starting with a semi-elliptical crack front, it turns into a straight crack front after the crack reaches a depth of 3 mm, this describes the phenomenon that the multiple cracks existing in the specimen unite to a continuous crack front. Fischer and Fricke have shown that the results of this approach are in good accordance with experimental results [20]. For the calculation of SIFs in a semi-elliptical crack starting from the surface of a plain plate, Newman and Raju defined an empirical equation for the stress-intensity factors. The coefficients and their descriptions can be found in Appendix C, the standard solution for the M is depicted here [21]:

$$M = \left(M_1 + M_2 * \left(\frac{a}{T}\right)^2 + M_3 * \left(\frac{a}{T}\right)^4 \right) * \frac{f_w * f_\Phi * g}{Q} \tag{8}$$

The factors f_w, f_π, g and Q are used to determine the magnification factor for a crack in a plane plate. Considering the shape of the crack, the finite dimensions of the plate and the position within the crack at which the SIFs should be calculated. For the deepest point of the crack, this position is $\phi = \pi/4$ [21]. The analytical solutions for the specific geometric case M_k are defined by Bowness and Lee, see Appendix E [17].

Regarding the range of validity for the correction factor M by Newman and Raju, the condition $c/b < 0.5$ exists. For a straight crack front $c = b$, the condition is violated and the analytic solutions are out of their validity range [21]. Therefore, the 3D weight functions M and M_k should only be used for $a \leq 3$ mm. For $a > 3$ mm, the 2D weight functions from BS7910 should be used [7]:

$$M = 1.12 - 0.38 * \left(\frac{a}{T}\right) + 10.6 * \left(\frac{a}{T}\right)^2 - 21.7 * \left(\frac{a}{T}\right)^3 + 30.4 * \left(\frac{a}{T}\right)^4 \tag{9}$$

$$M_k = C_{Mk} * \left(\frac{a}{t}\right)^{k_{Mk}} \tag{10}$$

$$M_k \geq 1 \tag{11}$$

3. Material and experimental procedure

3.1. Material

To exclude the effects of material related uncertainties in the specimens, two different ferritic steel grades are examined in this study. One is S235J2 + N and the other is S500G1 + M, the Youngs modulus and the Poisson's ratios are identical for both steel grades, $E = 206$ GPa and $v = 0.3$. The chemical compositions for the BM can be seen in Table 1,

Table 1
Chemical composition of S235J2 + N and S500G1 + M used [w%] [22].

	C	Si	Mn	P	S	N	Cu
S235J2 + N	0.107	0.176	1.02	0.014	0.001	<0.001	0.016
S500G1 + M	0.056	0.208	1.58	0.012	0.002	0.004	0.273
	Mo	Ni	Cr	V	Nb	Ti	Al-T
S235J2 + N	0.002	0.020	0.023	0.001	<0.001	<0.001	0.041
S500G1 + M	0.175	0.516	0.056	0.001	0.020	0.001	0.033

Table 2
Results of the Charpy notch impact testing [8].

		BM	HAZ	WM
S235J2 + N	T27J	−78 °C	−79 °C	−28 °C
S500G1 + M	T50J	−119 °C	−85 °C	−39 °C

due to the welding process, a slightly different local composition of the material in the WM and HAZ can be expected.

In this study, the FCG is investigated below the RT but above the FTT, which requires identifying the lower temperature limit. To determine the FTT from the DBTT, the empirical relationship by Alvaro is used, see Formula (1). The DBTT is specified in the form of the T_{27J} criterion for S235 and the T_{50J} criterion for S500. For both materials Charpy impact tests have already been carried out by Braun et al. furthermore, the specimens used in this study were welded in the same setup [8]. The comparability of this is reduced because butt-welded joints were investigated, which are composed of multiple weld layers and thus repeated heat influx. In addition to the investigation of the BM, Braun et al. also carried out Charpy impact tests for material in the HAZ and the WM, his results are depicted in Table 2 [8].

The C and m parameters provided by the IIW recommendations and the BS7910 define the mean line with two times the standard deviation (SD) [6,7]. The corresponding Paris–Erdogan parameters for the mean line without the SD can be found in King, which are used in the following [15]. The parameters are valid for the BM or WM of ferritic steels tested in air, without further distinctions between steel grades and sub-zero temperature levels. In BS7910, a range of validity for the parameters is given for temperatures < 100 °C [7]. For the HAZ no Paris–Erdogan parameters are available, for a similar case Song et al. used the BM parameters for the HAZ [12]. After comparing the simplification with BM parameters with the use of WM parameters, the same assumption is used in this study.

The procedure for the determination of C and m parameters requires conducting multiple decreasing ΔK experiments, i.e., described in ASTM 647-15 [23]. According to this procedure, Sallaba et al. conducted decreasing ΔK experiments at RT for the BM and the WM of
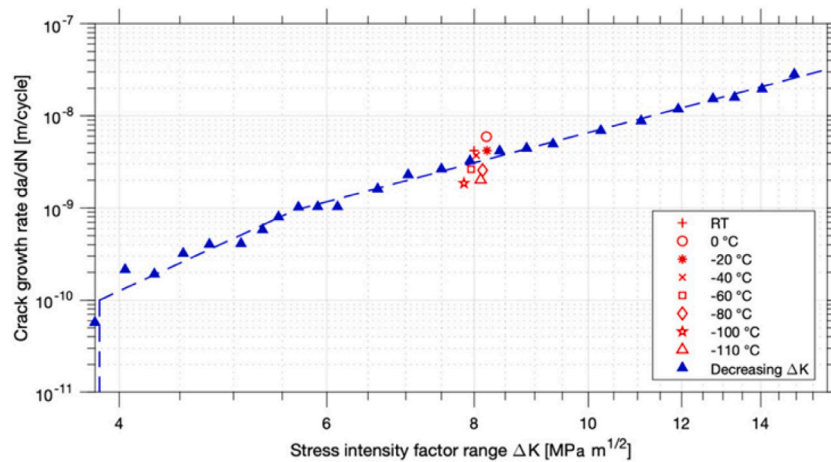
Fig. 5. Results of constant ΔK experiments at different temperatures and a decreasing ΔK experiment for S235 BM [25].

the steel grades S235 and S500, from which the C and m parameters can be derived [24,25]. Following ASTM 647-15 this procedure has to be conducted for every temperature level to determine the Paris–Erdogan parameters. Because the determination of C and m parameters was not the main scope of the study Sallaba et al. conducted just one constant ΔK experiment for each of the seven different sub-zero temperature levels [25]. One of the resulting plots is shown in Fig. 5. From the slope of the decreasing ΔK experiment at RT the m parameter is determined and from the one measuring point the C parameter for the specific temperature level. The one measuring point is sufficient to determine a C parameter, according to the observation by Alvaro the slope m can be assumed to be constant over temperature ranges but neglects the sensitivity for measurement errors [1].

In Sallaba et al. the tests of both the BM and the WM were carried out at stress ratios of $R = 0.5$ [24,25]. A stress ratio of $R = 0.5$ is commonly used to express the residual stresses of as-welded constructions, so the Paris–Erdogan parameters are well-suited for predicting crack growth [15]. The Paris–Erdogan parameters used in this study are depicted in Appendix A.

3.2. Specimen

The C-joints as well as the transverse stiffener specimens are made of three steel plates and connected over single-layered welds. The used welding technique is flux cored arc welding. For the welding process, a 1.2 mm diameter Outershield 71E-H wire is used in the S235 material and a Stone megafil 821r wire for the S500 material. The resulting plates have dimensions of 1000 mm x 500 mm with a plate thickness of 10 mm. The specimens are produced by cutting the plates with a hydraulic saw in pieces of 50 mm width by a length of 500 mm, after the sawing process the specimens are deburred [22].

3.3. Measurement of the geometry of the specimens

A central part of this study is the modelling of the crack growth of experimental specimens based on analytical solutions and the Paris–Erdogan equation. To use them, the local geometries of the specimens and their misalignments have to be known, as the latter influence the stress distribution. To compensate for their influence on the stress distribution, correction factors must be determined. These correction factors should compensate for secondary bending effects on the stress which emanate from angular misalignment ϕ and axial misalignment e. To measure the misalignments, two dial gauges are used in a measuring setup according to Fischer [26].

The procedure to determine a resulting stress magnification factor k_m is described in the IIW Recommendations, see [6]. The stress

magnification factor k_m consists of an axial part $k_{m,e}$ and an angular part $k_{m,a}$. Further information is found in the IIW Recommendations [6]. However, it should be noted that the clamping effects are not taken into account in these formulas, therefore the resulting secondary bending stress effects can be slightly overestimated [8]. The central equation to calculate the magnification factor k_m is:

$$k_m = 1 + (k_{m,e} - 1) + (k_{m,a} - 1) \tag{12}$$

The local weldment geometry for the standard solutions has been generated by laser triangulation and the curvature method by Schubnell et al. [27].

3.4. Setup of the fatigue experiment

For the experimental determination of the fatigue behaviour, a Schenck Horizontal Resonance Testing Machine with a maximum load capacity of 200 kN and a frequency of around 33 Hz is used. A specimen is applied with a constant amplitude cyclic load and the number of cycles to failure is measured. The specimens are tested at different stress amplitudes, with a stress ratio of $R = 0$. For the sub-zero experiments, the resonance testing machine is adapted with a climate chamber that separates specimen grips and specimen against the environment. The climate chamber allows it to set a temperature range between -180 °C to 280 °C. The cooling of the climate chamber is done by injecting vaporised nitrogen from a tank into the climate chamber. The temperature is continually measured by a PT100 platinum measuring resistor, based on the chamber temperature output, the injection of the nitrogen is controlled. With this setup, a constant chamber temperature of around ±1 °C can be maintained. Since the temperature within the chamber is not identical to the specimen temperature, another PT100 platinum measuring resistor is attached with a magnet to the specimen. The temperature thus measured is used for the experimental setting and evaluation. In Figure 6 (a) the complete setup and in Fig. 6(b) the climate chamber with the clamped specimen and PT100 platinum measuring resistor is shown.

4. Evaluation form of predicted and experimental fatigue lives

In this study, the results of 136 fatigue experiments are considered, which are divided into 12 different test series. A test series is used to examine the fatigue behaviour of one combination of weldment type, temperature level and steel grade. With the measured geometry data and the analytical formulas, for each of the 136 specimens the SIF range over the incremental crack growth steps are calculated. By solving the Paris–Erdogan Eq. (3) with appropriate Paris–Erdogan parameters, the analytically expected fatigue life of the specimens can be calculated.
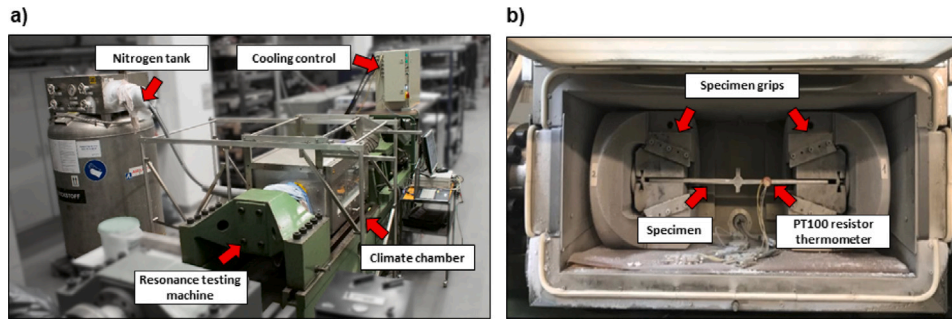
Fig. 6. (a) Complete experimental setup [28] (b) Climate Chamber [22].

Several Paris–Erdogan parameter sets can be found in Appendix A, defining either an unspecific ferritic steel or are determined for a specific steel and a temperature level. In this study, the suitability of these Paris–Erdogan parameter sets should be evaluated. Therefore, for each test series, multiple fatigue life predictions are made. To be able to compare predictions from various Paris–Erdogan parameter sets, a suitable presentation form is needed, which is outlined in the following.

For each specimen, the fatigue life has been determined experimentally and can be predicted by using a Paris–Erdogan parameter set. The results for a test series are plotted on a double logarithmic scale, the experimental fatigue lives on the y-axis and the predictions on the x-axis. If prediction and experiment perfectly coincide, a data point is on the 1:1 line. Accordingly, the greater the distance of a point from the 1:1 line, the worse the prognosis. By using the method of least squares to form a first-order best-fit line for the data points of one test series, the mean prediction accuracy for a Paris–Erdogan parameter set can be determined. An advantage of comparing the fatigue lives in logarithmic space is that the slope of the first-order best-fit line depends only on the Paris–Erdogan parameter m, while the intersection depends on both parameters C and m. This allows a separate validation of the Paris–Erdogan parameters C and m. The property of the first-order best-fit line is resulting from the structure of the Paris–Erdogan function:

$$\frac{da}{dN} = C * (\Delta K)^m \tag{13}$$

$$N_{f,analytic} = \int_{a_i}^{a_f} \frac{da}{C * (\Delta K)^m} \tag{14}$$

$$N_{f,analytic} = \frac{a_f - a_i}{C * (\Delta K)^m} \tag{15}$$

$$\log(N_{f,analytic}) = \log(a_f - a_i) - \log(C) - \log(\Delta K) * m \tag{16}$$

The extended Paris–Erdogan equation is used with the least-squares method to form a best-fit line of the first order for the predicted fatigue lives, it follows:

$$\log(N_{f,analytic}) = \alpha_1 * \log(N_{f,analytic}) + \alpha_0 \tag{17}$$

Here, α_0 and α_1 are the coefficients of the best-fitting straight line through the experimental data, defining deviation and slope. According to the least-squares method, they are the coefficients at which the square of the residuals (the difference between a data point and the fitted model value) r_i over the number of measured data n becomes minimal:

$$r_1 = \alpha_1 * \log(N_{f,analytic,1}) + \alpha_0 - \log(N_{f,exp,1}) \tag{18}$$

$$\vdots$$

$$r_n = \alpha_1 * \log(N_{f,analytic,n}) + \alpha_0 - \log(N_{f,exp,n}) \tag{19}$$

$$\min_{\alpha_0,\alpha_1} \sum_{i=1}^{n} r_i^2 \tag{20}$$

By solving the equation of the least square method it follows for α_0 and α_1:

$$\alpha_0 = \overline{\log(N_{f,exp})} - \alpha_1 * \overline{\log(N_{f,analytic})} \tag{21}$$

$$\alpha_1 = \frac{\sum_{i=1}^{n} \left(\log(N_{f,analytic,i}) * \log(N_{f,exp,i})\right) - n * \overline{\log(N_{f,analytic})} * \overline{\log(N_{f,exp})}}{\left(\sum_{i=1}^{n} (\log(N_{f,analytic,i}))^2\right) - n * \overline{\log(N_{f,analytic})}^2} \tag{22}$$

Each predicted fatigue life $N_{f,analytic,i}$ via the analytical solution and the Paris–Erdogan parameters are assigned to a point on the first order best-fit line. This point represents a "corrected" experimental fatigue life $N_{f,exp,i}$ determined by the least square method, see Fig. 7(a). Because the corrected experimental fatigue lives $N_{f,exp,i}$ all lay on the first-order best-fit line, the single fatigue life can be described with an equation in the form of the Paris–Erdogan function.

By extending the Paris–Erdogan equation with a logarithm, the only product of the Formula (16) is the $\log(\Delta K) * m$ term. Together with the structure of the formula for α_1, it follows that this coefficient depends only on the $\log(\Delta K) * m$ term. Accordingly, the slope of the first-order best-fit line depends only on the Paris–Erdogan parameter m, while the variable α_0, responsible for the intersection, depends on both parameters C and m. A perfect agreement of the predicted fatigue lives with the ones corrected via the least square method exists if the first-order best-fit line coincides with the 1:1 line in logarithmic space, i.e., $\alpha_1 = 1$ and $\alpha_0 = 0$. It is possible for only one C and m set and so allows their validation. In Fig. 7(b) can be seen that for a non-suitable C parameter with a correct m parameter, the best-fit line and the 1:1 line are parallel, while for a non-suitable m parameter, the slope and the deviation have changed.

5. Results

In this section, the accuracy of Paris–Erdogan parameters is examined by comparing predicted and experimentally determined fatigue lives. The C and m parameters used are listed in Table 4. The parameters for not further defined ferritic steels are taken from King and the materials-specific and temperature-specific parameters from Sallaba et al. [15,25,28].

5.1. Weld root failure of the C-joint at RT

In Fig. 8(a, b) the experimental fatigue lives for the C-joint at RT are plotted against the predicted fatigue lives, determined with different C and m parameters. Fig. 8(a) shows that by using the specific Paris–Erdogan parameters of the WM as well as the unspecific from King a good prediction for the experimental results was achieved. The predicted specific values for the S500 specimens in Figure 8 (b) are close to the 1:1 line, whereas the best-fit line from the standard parameters has a high deviation of the slope, i.e., the parameter m does not fit.
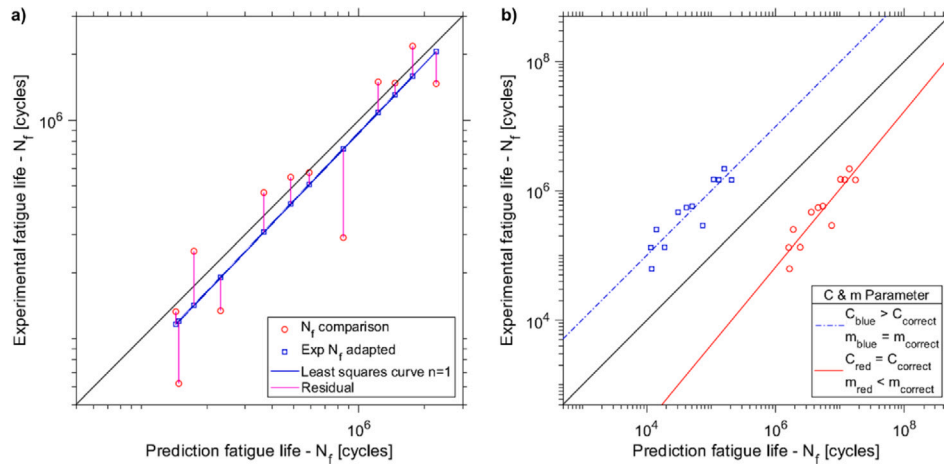
Fig. 7. First-order best-fit lines (a) with residuals (b) with two *C* & *m* parameter sets.
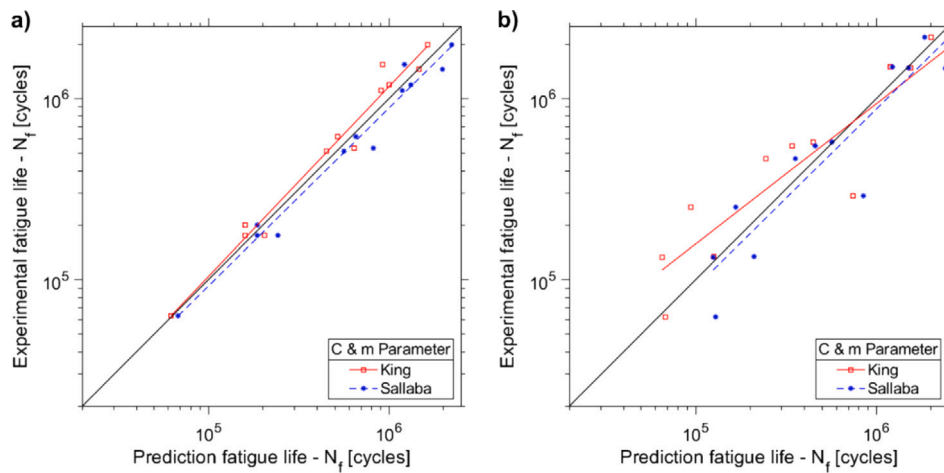

Fig. 8. Comparison of predicted and experimental fatigue lives at RT (a) for S235 C-joints (b) for S500 C-joints.

5.2. Weld toe failure of the transverse stiffener at RT

In Fig. 9(a, b) the experimental fatigue lives for the transverse stiffener at RT are plotted against the predicted fatigue lives, using different sets of *C* and *m* parameters. In Fig. 9(a) the best-fit lines for the S235 specimens are compared. It can be seen that the fatigue lives predicted with the two parameter sets are underestimated, whereby the fatigue live prediction with the parameter by King is closer to the experimentally determined values [15]. The high deviation of the specific best-fit line to the 1:1 line, especially regarding the slope, indicates that the parameters, from the constant ΔK experiments by Sallaba et al. do not represent the actual material behaviour [25]. For the S500 specimens depicted in Fig. 9 (b) a comparable coincidence between the 1:1 line and the best-fit lines are reached for the two parameter sets.

5.3. Weld root failure of the C-joint at sub-zero temperatures

Fig. 10 (a, b, c) compares the experimental with the predicted fatigue lives at three different experimental temperature levels RT, −20°C and −50°C, whereby the used material-specific *C* and *m* parameters are determined for both steel grades. It can be seen that for both steel grades, the coincidence of the best-fit lines with the 1:1 line is highest for the experiments at RT. The best-fit lines for the experiments at −20°C and −50°C show deviations from the 1:1 line, the mean predicted fatigue life is lower than the experimental determined. The stratification of the best-fit lines

for both steel grades is going from the RT to the −20°C line and then to the −50°C line. In the test series of the S235 C-joints at −50°C one specimen shows a brittle fracture surface, see Fig. 11, the other nine specimens have ductile fracture surfaces. Neglecting this data point, the slopes of the best-fit lines change only slightly between the temperature levels, see Fig. 10(b). The plots for S235 and S500 differ in the fact that the displacements of the S500 specimen's best-fit lines are smaller than for the best-fit lines of the S235 specimens, due to the agreement in the ordering it can be assumed that the behaviour of the S500 specimens is similar to that of the S235 specimens. Because there are no Paris–Erdogan parameters for S235, the following investigations are limited to S500 specimens.

Fig. 12 contains the results of three S500 C-joint test series conducted at RT, −20°C or −50°C in comparison with the predicted fatigue lives. For the predicted fatigue lives three different Paris–Erdogan parameter sets are applied which are valid for the corresponding experimental temperature in S500 WM. An exception is the temperature level of −50°C, because no material-specific *C* parameter was determined, the average of the *C* parameters for −40 °C and −60 °C is used. According to Sallaba et al. a constant *m* parameter of 2.36 is used for all temperature levels [25].

The best-fit lines for all three test series coincide largely with the 1:1 line, indicating good forecast accuracy. The deviations for −20°C and −50°C are slightly higher than for RT. The slope of the best-fit lines for RT and −50°C coincides well with the 1:1 line, while the best-fit line for −20°C has a slightly different slope despite the same *m* parameter.
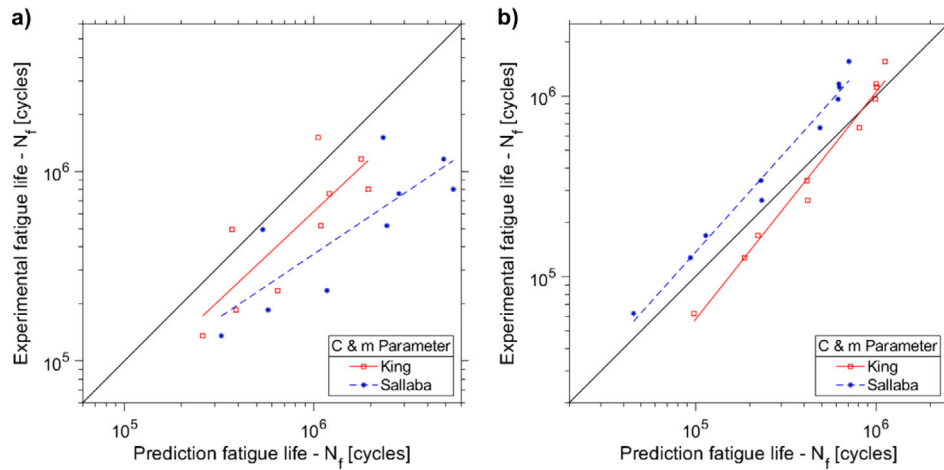
Fig. 9. Comparison of predicted and experimental fatigue lives at RT (a) for S235 Transverse stiffener (b) for S500 Transverse stiffener.
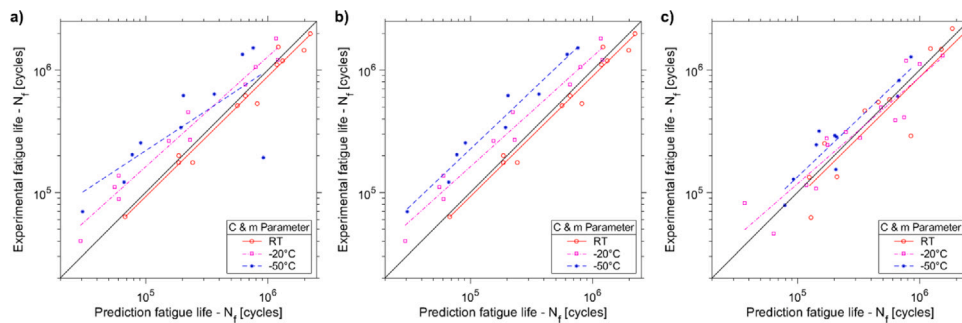

Fig. 10. Comparison with the experimental fatigue lives conducted at three temperature levels using one Paris–Erdogan parameter set obtained from room temperature tests for (a) S235, (b) S235 neglecting the outlier and (c) S500 steel specimens.
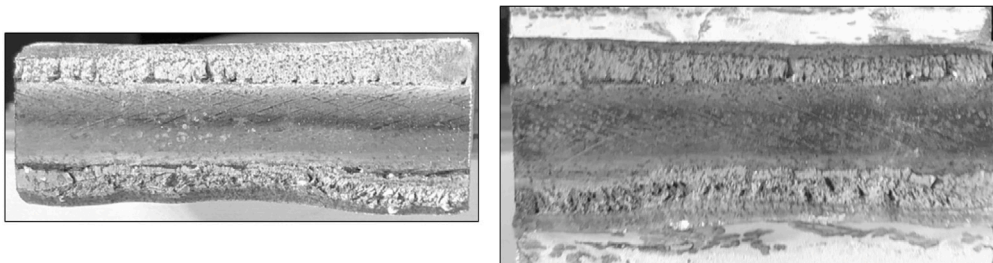

Fig. 11. Fracture surface of one S235 C-joint specimen tested at −50°C with characteristics of brittle crack growth.

5.4. Weld toe failure of the transverse stiffener at sub-zero temperatures

In Fig. 13 (a, b) the experimental and predicted fatigue lives of three test series at RT, −20°C and −50°C for S235 and S500 specimens are compared, using for each grade one set of C and m parameters, valid for the BM at RT. Whereby for the S235 specimens in Fig. 13(a) the values from King are used because Fig. 9(a) shows that the material-specific parameters from the experiments by Sallaba et al. do not represent the actual material behaviour [15,24]. For the S500 specimens the material-specific parameters for RT are used, see Fig. 13(b). The best-fit lines of both plots show a similar stratification following the experimental temperature from RT to −50°C, whereby the displacements between the S500 best-fit lines are smaller than between the S235 lines. The displacements of the best-fit lines for the experiments at −20°C and −50°C from the RT best-fit line are increasing. This indicates that with the decreasing temperature level the experimentally determined fatigue lives increase compared to the predicted fatigue lives. Thus for the S500 specimens, the coincidence of the best-fit lines with the 1:1 line

is highest for the experiments at RT and for the S235 specimens, the degree of underestimation is decreasing with the temperature.

In Fig. 14, the fatigue lives from three different test series of S500 transverse stiffeners are compared with the predicted fatigue lives. The test series differ in the experimental temperature of either RT, −20°C or −50°C. For the prediction of the fatigue lives a constant m parameter and three different C parameters are used, valid for RT, −20°C or −50°C. The C parameter for −50°C is not available, therefore the average of the C values for −40 °C and −60 °C is created.

The best-fit lines show a high degree of coincidence with each other, whereby they show a noticeable deviation from the 1:1 line. With regard to the slope, the best-fit lines are approximately parallel to the 1:1 line, which indicates the suitability of the m parameter of 3.38 which is constant for all temperature levels.

Table 3

Standard deviation with adapted and non-adapted C parameters from the best-fit line for RT.

Weldment type	Weld material	Exp. Temp.	$SD_{C,non-adapted}$	$SD_{C,adapted}$	$SD_{C,non-adapted}/SD_{C,adapted}$
C-joint	WM	−20°C	0.1711	0.1795	0.95
		−50°C	0.1843	0.1575	1.17
Transverse stiffener	BM	−20°C	0.0819	0.0791	1.04
		−50°C	0.1666	0.1416	1.18
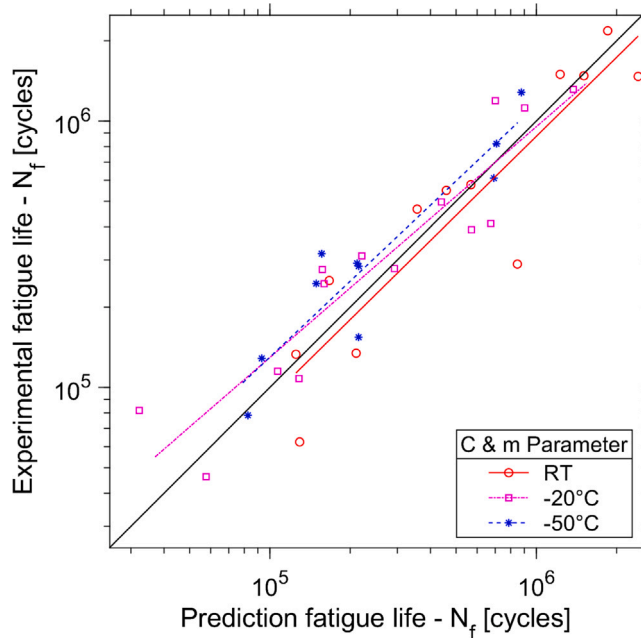
Fig. 12. Comparison of experimental and predicted fatigue lives using Paris–Erdogan parameter sets valid for the corresponding experiment at RT, −20°C and −50°C.

6. Discussion

Before the influences of the temperature level and the material on the prediction accuracy can be investigated, the validity of the used model and the parameters must be confirmed. For this purpose, test series of the specimens at RT are used, together with fatigue life predictions via the Paris–Erdogan parameters of King, which are the basis for standards and guidelines [15]. Figs. 8 and 9 show that a prediction is possible using specific determined parameters as well as parameters referred to in standards.

The 1:1 line does not show complete agreement with the best-fit lines generated by the Paris–Erdogan parameters that are specific to the material and temperature. The same applies for the best-fit lines derived from the parameters in the standards they also do not align with the 1:1 line. This small deviations can be attributed to a combination of factors, the limited number of tests per test series, non-matching C and m parameters, and the limitations of the traditional Paris–Erdogan equation when compared to more detailed models like the NASGRO equation.

The deviation already existing at RT does not limit the validity of the experiments at −20°C and −50°C, because, except for the experimental temperature, all experiments were carried out under the same conditions. The specimens come from the same batch and were tested in the same experimental setup. The deviations resulting from individual experimental settings and geometric deviations are assumed to be statistically distributed, which means that the only significant difference between the test series is the experimental temperature.

Figs. 10 and 13 depict a comparison of three temperature levels using a Paris–Erdogan parameter set acquired at RT. It is assumed that the Paris–Erdogan parameters have the same degree of validity

for all three temperature levels, suggesting a high degree of coincidence among the three levels. Instead, a stratification of the best-fit lines can be seen, indicating that as the temperature level decreases, the prediction with the Paris–Erdogan parameters determined at RT becomes more conservative. This aligns with the current understanding that the fatigue strength increases as the temperature decreases until it falls below the FTT, see Braun [4]. The stratification of the best-fit lines confirms that the accuracy of predictions using a Paris–Erdogan parameter set decreases as the temperature decreases, as the increase in fatigue strength is not accounted for.

To investigate if the decreasing prediction accuracy can be compensated, C and m parameters valid for RT, −20°C and −50°C are applied to the corresponding S500 test series, see Fig. 12 for the C-joints and Fig. 14 for the transverse stiffeners. At this point, it is investigated if there is a better prediction accuracy compared to the best-fit lines in Fig. 10(c) and Fig. 13(b) using non-adapted parameters. To quantify the degree to which the forecast accuracy has been changed, the coincidence of the best-fit lines for −20°C and −50°C to the best-fit line for RT is quantified with the least square method.

The first-order best-fit lines are defined by minimising the square of the residuals r_i over the number of measured data n, see Fig. 7(a). The best-fit lines for sub-zero temperatures are compared with the best-fit line for RT. For every data point of the sub-zero experiments, the logarithmic distance to the best-fit line for RT is calculated, i.e., the residuals. From these residuals, the SD of the test data and the C parameter is determined, see (23). If the coincidence of a best-fit line with adapted C increases compared to the best-fit line with non-adapted C, this results in lower SDs

$$SD = \sqrt{\frac{\sum_i^n (\log(N_{f,adapted,RT,i}) - \log(N_{f,comparison,i}))^2}{n}} \tag{23}$$

The results are shown in Table 3:

Examining the results in Table 3, it can be seen that the best-fit lines of the adapted and non-adapted C parameters for −20°C differ only slightly. For the S500 WM, there is a small decrease in the agreement and for the S500 BM a small improvement in the agreement. On the other hand, a significant increase in the agreement of the adapted C parameters compared to the non-adapted ones can be observed for the best-fit lines of the experiments at −50°C. The adapted C parameters show a 17% higher agreement for the C-joint and an 18% higher agreement for the transverse stiffener. The only small and at the same time non-uniform differences in the SD for −20°C for S500 indicate that there are still no significant temperature influences on the fatigue behaviour in this temperature range. Whereby, it should be noted, that the identification of small changes in fatigue behaviour due to temperatures at −20°C would require correspondingly large test series, which were not available in this work. Because of the small differences in the SD, the Paris–Erdogan parameters for RT should be suitable for predicting the fatigue life of S500 specimens at −20°C. The larger differences and the uniform results for C-joints and transverse stiffeners for the SDs at −50°C of C-joints and transverse stiffeners, on the other hand, indicate noticeable temperature dependent influences. The results in Table 3 show that by using adapted C parameters, these temperature dependent influences can be taken into account in the prediction of fatigue lives.

From the comparison between the test data for S235 and S500 specimens in Figs. 10 and 13, follows that the shifts between the temperature levels for the S235 are higher than for the S500 specimens. It is expected that with the use of temperature adapted C parameters,

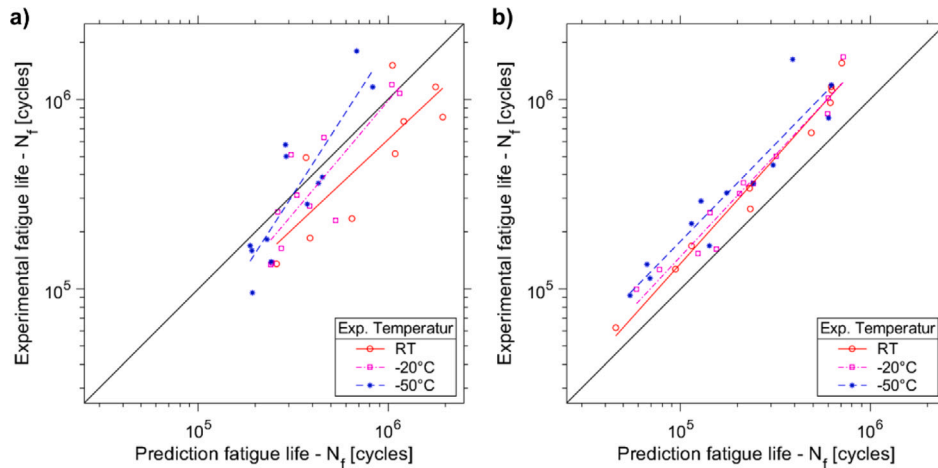**Fig. 13.** Comparison with the experimental fatigue lives conducted at three temperature levels using one Paris–Erdogan parameter set obtained from room temperature tests for (a) S235 and (b) S500 steel specimens.
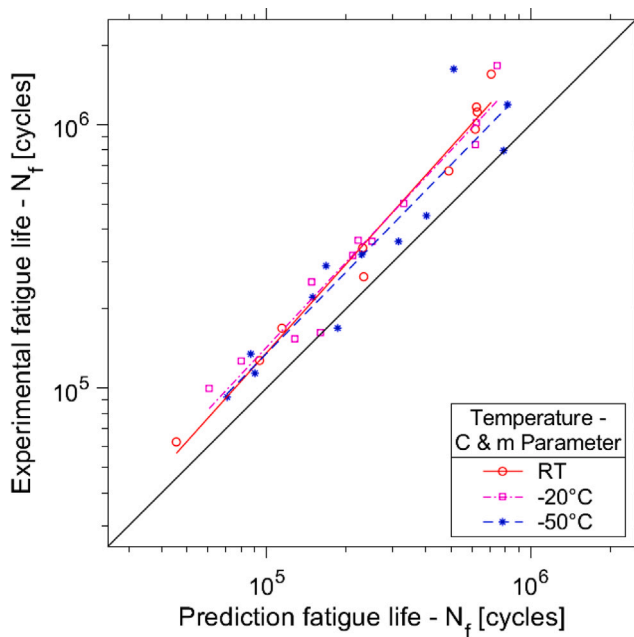

Fig. 14. Comparison of experimental and predicted fatigue lives using Paris–Erdogan parameter sets valid for the corresponding experiment at RT, −20°C and −50°C.

especially for parts made of low-strength S235, high improvements in the prediction accuracy of the fatigue life can be achieved and the over-dimensioning can be reduced.

The presentation format with which the predictions of the different C and m parameter sets have been compared makes it possible to easily identify outliers in a set of fatigue experiments. One such outlier is shown in Fig. 10(a), for a S235 specimen with root failure at −50°C the predicted fatigue life is significantly higher than the experimentally determined fatigue life. Whereas for the other nine measurements of the test series, the predicted fatigue lives are smaller than experimentally determined, which fits with the observations by Alvaro that the fatigue life increases with lower temperatures [1]. A possible explanation for this outlier is that the crack growth happened below the FTT, while the other nine failed above the FTT. According to the assumed correlation between the FTT and the DBTT, the FTT is 15°C to 20 °C below the DBTT, which is defined by the T_{27J} value, for S235 WM −28 °C [10,29]. The fracture surface depicted in Fig. 11 shows the typical characteristics

of a brittle fracture together with the T_{27J} value it can be stated that the specimen failed below the DBT. The experiments were conducted close to the predicted FTT but for the more far-reaching assumption that the FCG had taken place below the FTT, the fracture surface would have had to be examined with an electron microscope.

Under the assumption that the one outlier specimen failed below the FTT, the question is why just one specimen is below the FTT and nine are above the FTT, despite nearly identical test parameters. For example, the temperature in the climate chamber only fluctuates within a range of ±1 °C, with even smaller fluctuations in the temperature of the specimen. Other possible influencing factors for the scatter are the inhomogeneity of the material due to the directional solidification of the weldment or different residual stresses between the specimens [4]. However, a comprehensive explanation does not yet exist. Regardless of the explanatory approach, if there is a wide temperature range around the assumed FTT for which both ductile and brittle fatigue behaviour is possible, there is a large uncertainty in the selection of the Paris parameters C and m. Averaging between the results of ductile and brittle failure is not useful, it is mandatory to use the conservative Paris parameters, i.e., parameters for brittle failure. This results in over-dimensioning for the majority of welds sized for applications close to FTT. Regarding the sub-zero temperature levels above the FTT, Table 3 shows that the Paris–Erdogan parameters in the standards are too conservative and should therefore consider the low-temperature behaviour.

7. Conclusions

Based on the investigations carried out, it could be shown that the prediction accuracy decreases when Paris–Erdogan parameters determined at RT are also applied to the sub-zero temperature level. However, it could also be shown that the decrease in the prediction accuracy could be compensated when material and temperature-specific Paris–Erdogan parameters are used. In the investigated sub-zero temperature level, a stronger increase in fatigue strength was found for specimens made of low-strength S235 than for specimens made of high-strength S500. Accordingly, the potential in the prediction accuracy is greater for parts made of S235, which can be realised by taking into account the temperature-specific Paris–Erdogan parameters. The method used in this work to assess the prediction accuracy via first-order best-fit lines has allowed an easy association of deviations in the prediction to either the C or the m parameter. It also made it possible to quickly identify outliers in the test series.

CRediT authorship contribution statement

Nils-Erik Sanhen: Conceived and designed the analysis, Collected the data, Contributed data or analysis tools, Performed the analysis, Wrote the paper. **Moritz Braun:** Contributed data or analysis tools, Wrote the paper.

Declaration of competing interest

The authors declare that they have no known competing financial interests or personal relationships that could have appeared to influence the work reported in this paper.

Data availability

Data will be made available on request.

Appendix A. Paris–Erdogan parameters

See Table 4

Appendix B. Formulas for the 2D Mk coefficients following BS7910

$$\lambda_0 = 0.956 - 0.343 * \left(\frac{W}{T} \right) \tag{24}$$

$$\lambda_1 = -1.219 + 6.21 * \left(\frac{H}{T} \right) - 12.22 * \left(\frac{H}{T} \right)^2 + 9.704 * \left(\frac{H}{T} \right)^3 - 2.741 * \left(\frac{H}{T} \right)^4 \tag{25}$$

$$\lambda_2 = 1.954 - 7.938 * \left(\frac{H}{T} \right) + 13.299 * \left(\frac{H}{T} \right)^2 - 9.541 * \left(\frac{H}{T} \right)^3 + 2.513 * \left(\frac{H}{T} \right)^4 \tag{26}$$

Appendix C. Formulas for the M coefficients in Newman and Raju

$$M_1 = 1.13 - 0.09 * \left(\frac{a}{c} \right) \tag{27}$$

$$M_2 = -0.54 + \left(\frac{0.89}{0.2 + \left(\frac{a}{c} \right)} \right) \tag{28}$$

$$M_3 = 0.5 - \left(\frac{1}{0.65 + \left(\frac{a}{c} \right)} \right) + 14 * \left(1 - \left(\frac{a}{c} \right) \right)^{24} \tag{29}$$

$$f_w = \sqrt{ \sec \left(\frac{\pi}{2} * \frac{c}{b} * \left(\frac{a}{T} \right)^{0.5} \right) } \tag{30}$$

$$f_\Phi = \left(\left(\frac{a}{c} \right)^2 * \left(\cos \left(\frac{\pi}{4} \right) \right)^2 + \left(\sin \left(\frac{\pi}{4} \right) \right)^2 \right)^{0.25} \tag{31}$$

$$g = 1 + \left(0.1 + 0.35 * \left(\frac{a}{T} \right)^2 \right) * \left(1 - \sin \left(\frac{\pi}{4} \right) \right)^2 \tag{32}$$

$$Q = \sqrt{ \left(1 + 1.464 * \left(\frac{a}{c} \right)^{1.65} \right) } \tag{33}$$

Where: f_w = finite width correction factor [21] f_Φ = an angular function from the embedded elliptical crack [21] g = correction factor depending on the crack depth and the position in the elliptical crack Q = shape factor for elliptical crack [21]

Appendix D. Formulas for the 3D Mk coefficients following BS7910

$$C_{Mk} = 0.8068 - 0.1554 * \left(\frac{H}{t} \right) + 0.0429 * \left(\frac{H}{t} \right)^2 + 0.0794 * \left(\frac{W}{t} \right) \tag{34}$$

$$k_{Mk} = -0.1993 - 0.1839 * \left(\frac{H}{t} \right) + 0.0495 * \left(\frac{H}{t} \right)^2 + 0.0815 * \left(\frac{W}{t} \right) \tag{35}$$

Appendix E. Formulas for the Mk parameter of the transverse stiffener

$$A_1 = -1.0343 * \left(\frac{a}{c} \right)^2 - 0.15657 * \frac{a}{c} + 1.3409$$

$$A_2 = 1.3218 * \left(\frac{a}{c} \right)^{-0.61153}$$

$$A_3 = -0.87238 * \frac{a}{c} + 1.2788$$

$$A_4 = -0.46190 * \left(\frac{a}{c} \right)^3 + 0.67090 * \left(\frac{a}{c} \right)^2 - 0.37571 * \frac{a}{c} + 4.6511$$

$$f_1 = 0.43358 * \left(\frac{a}{T} \right)^{A_1 + \left(A_2 * \frac{a}{T} \right)^{A_3}} + 0.93163 * \exp \left(\frac{a}{T} \right)^{-0.050966} + A_4$$

$$A_5 = -0.00038737 * \theta^2 + 0.64771 * \theta - 0.72368$$

$$A_6 = 0.24183 * \theta + 176.23$$

$$A_7 = -0.00027743 * \theta + 2.8143$$

$$f_2 = A_5 * \left(1 - \frac{a}{T} \right)^{A_6} + A_7 * \left(\frac{a}{T} \right)^{-0.10740 * \frac{a}{T}}$$

$$A_8 = -0.082502 * \theta^2 + 0.0084862 * \theta + 0.38417$$

$$A_9 = 0.010766 * \left(\frac{L}{T} \right)^3 - 0.060159 * \left(\frac{L}{T} \right)^2 + 0.13667 * \frac{L}{T} - 0.023400$$

$$A_{10} = -0.028378 * \left(\frac{L}{T} \right)^3 + 0.16489 * \left(\frac{L}{T} \right)^2 - 0.35584 * \frac{L}{T} - 0.00024554$$

Table 4
Material Properties.

Source	Material	Environment	Temperature	Units	C	m
King [15]	Steel - BM	Air	< 100 ° C [7]	K [N mm$^{-3/2}$] da/dN [mm/cycle]	1.5×10^{-13}	3
King [15]	Steel - WM	Air	< 100 ° C [7]	K [N mm$^{-3/2}$] da/dN [mm/cycle]	2.5×10^{-13}	3
Sallaba et al. [24]	S235 - BM	Air	RT	K [N mm$^{-3/2}$] da/dN [mm/cycle]	1.02×10^{-16}	4.2
Sallaba et al. [24]	S235 - WM	Air	RT	K [N mm$^{-3/2}$] da/dN [mm/cycle]	6.26×10^{-14}	3.2
Sallaba et al. [25]	S500 - BM	Air	RT	K [N mm$^{-3/2}$] da/dN [mm/cycle]	3.02×10^{-14}	3.38
Sallaba et al. [25]	S500 - WM	Air	RT	K [N mm$^{-3/2}$] da/dN [mm/cycle]	8.13×10^{-12}	2.36
Sallaba et al. [25]	S500 - WM	Air	−20 ° C	K [N mm$^{-3/2}$] da/dN [mm/cycle]	8.57×10^{-12}	2.36
Sallaba et al. [25]	S500 - WM	Air	−40 ° C	K [N mm$^{-3/2}$] da/dN [mm/cycle]	7.92×10^{-12}	2.36
Sallaba et al. [25]	S500 - WM	Air	−60 ° C	K [N mm$^{-3/2}$] da/dN [mm/cycle]	6.84×10^{-12}	2.36
Sallaba et al. [25]	S500 - BM	Air	−20 ° C	K [N mm$^{-3/2}$] da/dN [mm/cycle]	2.92×10^{-14}	3.38
Sallaba et al. [25]	S500 - BM	Air	−40 ° C	K [N mm$^{-3/2}$] da/dN [mm/cycle]	2.79×10^{-14}	3.38
Sallaba et al. [25]	S500 - BM	Air	−60 ° C	K [N mm$^{-3/2}$] da/dN [mm/cycle]	1.962×10^{-14}	3.38

$$A_{11} = -0.0015061 * \left(\frac{L}{T}\right)^2 + 0.023369 * \frac{L}{T} - 0.23124$$

$$A_{12} = 0.051554 * \theta^2 + 0.025447 * \theta + 1.8975$$

$$A_{13} = -0.12914 * \theta^2 + 0.21863 * \theta + 0.13798$$

$$A_{14} = -0.20136 * \left(\frac{L}{T}\right)^2 + 0.93311 * \frac{L}{T} - 0.41496$$

$$A_{15} = 0.20188 * \left(\frac{L}{T}\right)^2 - 0.97857 * \frac{L}{T} + 0.068225$$

$$A_{16} = -0.027338 * \left(\frac{L}{T}\right)^2 + 0.12551 * \frac{L}{T} - 11.218$$

$$f_3 = A_8 * \left(\frac{a}{T}\right)^{A_9*\theta^2+A_{10}*\theta+A_{11}} + A_{12} * \left(\frac{a}{T}\right)^{A_{13}} + \left(A_{14} * \left(\frac{a}{T}\right)^2 + A_{15} * \frac{a}{T} + A_{16}\right)$$

$$M_k = f_1 + f_2 + f_3$$

References

[1] A. Alvaro, O.M. Akselsen, X. Ren, A. Kaneko, Fundamental aspects of fatigue of steel in arctic applications, 2014, pp. 247–254,

[2] Lloyd's Register, Fatigue design assessment: FDA ice fatigue induced by ice loading, 2011.

[3] R. Bridges, S. Zhang, V. Shaposhnikov, Experimental investigation on the effect of low temperatures on the fatigue strength of welded steel joints, Ships Offshore Struct. 7 (3) (2012) 311–319, http://dx.doi.org/10.1080/17445302.2011.563550.

[4] M. Braun, Assessment of fatigue strength of welded steel joints at sub-zero temperatures based on the micro-structural support effect hypothesis (Dissertation), Technische Universität Hamburg, Hamburg, 2021.

[5] M. Braun, Statistical analysis of sub-zero temperature effects on fatigue strength of welded joints, Weld. World 66 (2021) 83, http://dx.doi.org/10.1007/s40194-021-01207-y.

[6] A.F. Hobbacher, Recommendations for Fatigue Design of Welded Joints and Components, Springer International Publishing, Cham, 2016, http://dx.doi.org/10.1007/978-3-319-23757-2.

[7] British Standards Institution, Guide to methods for assessing the acceptability of flaws in metallic structures: BS 7910:2013+a1:2015, 2015, URL https://www.academia.edu/33758342/Guide_to_methods_for_assessing_the_acceptability_of_flaws_in_metallic_structures.

[8] M. Braun, A. Kahl, T. Willems, M. Seidel, C. Fischer, S. Ehlers, Guidance for material selection based on static and dynamic mechanical properties at sub-zero temperatures, J. Offshore Mech. Arct. Eng. 143 (4) (2021) http://dx.doi.org/10.1115/1.4049252.

[9] A. Alvaro, O.M. Akselsen, X. Ren, B. Nyhus, Fatigue crack growth of a 420 MPa structural steel heat affected zone at low temperatures, in: J.S. Chung, M. Muskulus, T. Kokkinis, A. M. Wang (Eds.), 2019, URL https://www.researchgate.net/publication/332605098_Fatigue_Crack_Growth_of_a_420_MPa_Structural_Steel_Heat_Affected_Zone_at_Low_Temperatures.

[10] A. Alvaro, O.M. Akselsen, X. Ren, G. Perillo, B. Nyhus, On the relation between fatigue and static ductile to brittle transition for weld simulated 420 MPa structural steel, in: J.S. Chung, O. Gudmestad, M.S. Triantafyllou, T. Yao (Eds.), ISOPE - International Offshore and Polar Engineering Conference. Proceedings, International Society of Offshore & Polar Engineers, 2017, pp. 298–303, URL https://www.researchgate.net/publication/332605001_On_the_Relation_between_Fatigue_and_Static_Ductile_to_Brittle_Transition_for_Weld_Simulated_420_MPa_Structural_Steel.

[11] U. Zerbst, R.A. Ainsworth, H. Beier, H. Pisarski, Z.L. Zhang, K. Nikbin, T. Nitschke-Pagel, S. Münstermann, P. Kucharczyk, D. Klingbeil, Review on fracture and crack propagation in weldments – A fracture mechanics perspective, Eng. Fract. Mech. 132 (5) (2014) 200–276, http://dx.doi.org/10.1016/j.engfracmech.2014.05.012.

[12] W. Song, X. Liu, J. Xu, Y. Fan, D. Shi, M. He, X. Wang, F. Berto, Fatigue fracture assessment of 10CrNi3MoV welded load–carrying cruciform joints considering mismatch effect, Fatigue Fract. Eng. Mater. Struct. 44 (7) (2021) 1739–1759, http://dx.doi.org/10.1111/ffe.13457.

[13] C. Branco, S.J. Maddox, V. Infante, E.C. Gomes, Fatigue performance of tungsten inert gas (TIG) and plasma welds in thin sections, Int. J. Fatigue 21 (6) (1999) 587–601, http://dx.doi.org/10.1016/S0142-1123(98)00084-X.

[14] U. Zerbst, M. Madia, B. Schork, J. Hensel, P. Kucharczyk, D. Ngoula, D. Tchuindjang, J. Bernhard, C. Beckmann, Fatigue and fracture of weldments, Springer International Publishing, Cham, 2019, http://dx.doi.org/10.1007/978-3-030-04073-4.

[15] R.N. King, A review of fatigue crack growth rates in air and seawater: OTH-511, 1998.

[16] H.A. Richard, M. Sander, Fatigue Crack Growth: Detect - Assess - Avoid, in: Solid Mechanics and Its Applications, vol. 227, Springer International Publishing, Cham and s.l., 2016, http://dx.doi.org/10.1007/978-3-319-32534-7.

[17] D. Bowness, M.M. Lee, Fracture Mechanics Assessment of Fatigue Cracks in Offshore Tubular Structures, HSE Books, London, 2002, URL https://www.osti.gov/etdeweb/biblio/20270838.

[18] M. Braun, A.-S. Milaković, F. Renken, W. Fricke, S. Ehlers, Application of local approaches to the assessment of fatigue test results obtained for welded joints at sub-zero temperatures, Int. J. Fatigue 138 (2020) http://dx.doi.org/10.1016/j.ijfatigue.2020.105672.

[19] K.M. Engesvik, T. Moan, Probabilistic analysis of the uncertainty in the fatigue capacity of welded joints, Eng. Fract. Mech. 18 (4) (1983) 743–762, http://dx.doi.org/10.1016/0013-7944(83)90122-4.

[20] C. Fischer, W. Fricke, Simulation des zyklischen rissfortschritts- und der rissform an lasttragenden kreuzstößen, in: ANSYS Conference & 30th User's Meeting, 2012, URL https://www.researchgate.net/publication/263465528_Simulation_des_zyklischen_Rissfortschritts-_und_der_Rissform_an_lasttragenden_Kreuzstossen.

[21] J.C. Newman, I.S. Raju, An empirical stress-intensity factor equation for the surface crack, Eng. Fract. Mech. 15 (1–2) (1981) 185–192, http://dx.doi.org/10.1016/0013-7944(81)90116-8.

[22] M. Braun, R. Scheffer, W. Fricke, S. Ehlers, Fatigue strength of fillet–welded joints at subzero temperatures, Fatigue Fract. Eng. Mater. Struct. 43 (2) (2020) 403–416, http://dx.doi.org/10.1111/ffe.13163.

[23] ASTM International, ASTM 647-15: Standard test method for measurement of fatigue crack growth rates, 2016.

[24] F. Sallaba, Analysis of fatigue crack growth threshold of welded structural steel (Project thesis,), Technische Universität Hamburg, 2019.

[25] F. Sallaba, F. Rolof, S. Ehlers, C.L. Walters, M. Braun, Relation between the fatigue and fracture ductile-brittle transition in S500 welded steel joints, Metals 12 (3) (2022) 385, http://dx.doi.org/10.3390/met12030385.

[26] C. Fischer, Bewertung der Schwingfestigkeit von Schweißverbindungen mittels der Formänderungsenergiedichte (Dissertation), Institut für Konstruktion und Festigkeit von Schiffen und Technische Universität Hamburg-Harburg, Technische Universität Hamburg-Harburg, 2016.

[27] J. Schubnell, M. Jung, C.H. Le, M. Farajian, M. Braun, S. Ehlers, W. Fricke, M. Garcia, A. Nussbaumer, J. Baumgartner, Influence of the optical measurement technique and evaluation approach on the determination of local weld geometry parameters for different weld types, Weld. World 64 (2) (2020) 301–316, http://dx.doi.org/10.1007/s40194-019-00830-0.

[28] F. Sallaba, Investigation of fatigue ductile-brittle transition in steel and welded joints (Master thesis), Technische Universität Hamburg, 2020.

[29] C.L. Walters, A. Alvaro, J. Maljaars, The effect of low temperatures on the fatigue crack growth of S460 structural steel, Int. J. Fatigue 82 (7) (2016) 110–118, http://dx.doi.org/10.1016/j.ijfatigue.2015.03.007.